Nonlinear features and energy transfer in an Acoustic Black Hole beam through intentional electromechanical coupling

Linli Zhang [a], Gaetan Kerschen [b], Li Cheng [a],*

[a] *Department of Mechanical Engineering, The Hong Kong Polytechnic University Hung Hom, Kowloon, Hong Kong SAR, PR China*
[b] *Department of Aerospace and Mechanical Engineering, University of Liège Allée de la Découverte 9, B-4000 Liège, Belgium*

ARTICLE INFO

ABSTRACT

Acoustic Black Hole (ABH) phenomenon features unique wave retarding and energy focusing of flexural waves inside thin-walled structures whose thickness follows a power-law variation. Existing studies, mostly focusing on linear aspects, show the deficiency of the linear ABH structures in coping with low-frequency problems, typically below the so-called cut-on frequency. In this paper, electrical nonlinearities are intentionally imposed via PZT patches over an ABH beam to tactically influence its dynamics through electromechanical coupling. Using a fully coupled electromechanical beam model, typical electromechanical coupling phenomena between the beam and the external nonlinear circuits, as well as the resultant salient nonlinear features of the system, are numerically investigated. Results show the beneficial effects arising from the intentional electrical nonlinearity in terms of generating energy transfer from low to high frequencies inside the beam, before being dissipated by the ABH covered by a small amount of damping materials. As such, the effective frequency range of the ABH is broadened, conducive to low-frequency vibration control problems. Meanwhile, different from existing mechanical means, the introduced intentional electrical nonlinearity allows for flexible tuning to accommodate specific frequency ranges arising from different applications.

1. Introduction

Acoustic Black Hole (ABH) in thin-walled structures undergoing bending vibration exhibits some unique features, exemplified by the phase velocity reduction of the flexural waves and energy focalization. Since its inception [1], ABH concept has been arousing intense interests in the vibration and acoustic community, which accentuates at an accelerating pace during the last decade as reviewed by recent papers [2,3]. The design of an ABH structure is based on the tailoring of its thickness profile according to a reducing power-law relationship, so that the local phase and the group velocity of the flexural waves gradually reduce to zero when approaching the ABH tip where the structural thickness is near zero. This neutralizes wave reflection and causes high energy concentration at the ABH tip in the ideal scenario [4,5]. Although the aforementioned ideal process might be affected by the inevitable residual thickness at the ABH tip due to the limitation in machining, the adverse effect of the truncated thickness can be alleviated by using a small amount of viscoelastic coating over the tip area [6–9]. ABH phenomena have been exploited for realizing various functionalities for wave manipulation and other engineering applications. In addition to vibration reduction of structures [10,11], ABH-induced slow wave phenomena are shown to impair the supersonic structural wave components in a flexural vibrating structure, thus warranting a

---

* Corresponding author.
   E-mail address: li.cheng@polyu.edu.hk (L. Cheng).

reduced sound radiation efficiency which is beneficial for noise control applications [12,13]. The ABH-induced high energy concentration has also been exploited to conceive efficient energy harvesting devices [14,15].

ABH research started from simple 1D and 2D structures. Existing analysis methods include the geometrical acoustic approach [16,17], the transfer matrix approach [18,19] and energy-based semi-analytical approaches [20,21], mostly for simple benchmark systems. Finite Element Method (FEM) [22,23] is predominantly used for more complex structures. Meanwhile, experimental works [24–26] have also been carried out on a variety of beam-like and plate-like structures. With these numerical and experimental attempts, predominant ABH phenomena have been revealed, which greatly enriched our understanding on various aspects pertinent to ABH phenomena.

However, most existing analyses on ABH mainly focus on linear aspects [27,28]. Though exhibiting broadband features, typical ABH effects in linear systems only persist above the so-called cut-on frequency, defined in relation to the ABH dimension and the wavelength of the incoming waves [22,29]. Further reducing the frequency limit would require the use of exorbitantly large structures which may not be acceptable in practice. Therefore, how to reduce the effective frequency range of the ABH effects in a reasonably sized structure is seen to be a bottle-necking problem. Past attempts to tackle this problem include the use of extended platform over the thin part of the ABH structure for prolonging the ABH effect [10] and the design of helical ABH for increasing its effective length [30] etc. Leaving the limited improvement aside, such practice challenges the current manufacturing capability and compromises the acceptance of the structures.

The exploration of system nonlinearity, either inherently existing in a structure or intentionally added, might offer a useful solution to the problem. In fact, nonlinearity has been the focus of investigation for a variety of mechanical and physical applications including nonlinear vibration absorbers [31], shock isolation systems [32], energy harvesters [33] and nano- and micro-electromechanical systems [34], even metamaterials [35]. It is well-known that nonlinear systems generate harmonics [36], which are multiples of the excitation frequency. This dynamical mechanism has been exploited since several decades to transfer energy from low to high frequencies. For instance, Nayfeh *et al.* [37] utilized the saturation phenomenon to create nonlinearity which in turn transfers energy from a directly-excited and problematic vibration mode to a higher-frequency mode. As the forcing amplitude is increased, the response amplitude of the directly excited mode remains constant (*i.e.*, the mode saturates) whereas the response of the indirectly-excited mode increases. Nonlinear absorbers that feature vibro-impacts were also developed to transfer energy between structural modes [38].

However, a significant challenge is the practical realization of the sought nonlinearity. Mechanical nonlinearities such as cables [39] and springs [40] have some inherent limitations. As such, the practical relevance of these designs is questionable for real-life applications and the lack of tuning flexibility is also seen as a potential problem. This is why the electrical nonlinearity was proposed recently for developing novel nonlinear vibration absorbers [41]. Piezoelectric shunt damping has become a popular technique to reduce unwanted vibrations in structural systems. The technique relies on the transducing capability of a piezoelectric material, i.e., its ability to convert part of its mechanical energy into electrical energy, which is then be dissipated by connecting properly tuned shunt circuits to the transducer. In addition to linear shunt whose performance strongly relies on a precise tuning of the electrical resonant frequency, Agnes and Inman [42] investigated the effect of nonlinear shunts. Investigations show that the bandwidth of the piezoelectric absorber could be increased; however, undesirable nonlinear phenomena such as quasiperiodic and chaotic motions are also generated. Along the same lines, Richard *et al.* utilized continuous switching of a piezoelectric shunt to realize a nonlinear absorber [43]. Moreover, inspired by the nonlinear piezoelectric shunt technique [44–46], nonlinear digital oscillators were used on the uniform metamaterial beam for broadband micro-vibration attenuation [47].

Despite these efforts, there has been clearly a lack of effort made on ABH structures in view of drawing benefit from intentional nonlinearities. There exist only a few published papers on the topic, among which Denis *et al.* investigated the effects of the geometrical nonlinearities using a model based on a Von Karman plate [48], which suggest that possible geometrical nonlinearities inside the structures, due to the amplified large vibration amplitude within the high energy concentration area, are definitely present and affect the expected ABH effects [49]. Indeed, high amplitude vibration typically produces the coupling between the out-of-plane (flexural) and in-plane (longitudinal) motion of the structure, which in principle can lead to energy transfer between different frequency ranges. But the ABH wedge has to be long enough to induce noticeable geometrical nonlinearities, which is also seen as a limitation. Afterwards, contact nonlinearity was considered on an ABH beam. In particular, a vibro-impactor was used as a mean to generate nonlinearities in an ABH beam to create effective energy transfer effects [50]. The expected outcome of the process is to realize energy transfer from low to high frequencies, thereby enhancing the passive damping effect of the ABH beam at low frequencies and achieving vibration attenuation [51,52]. However, mechanical nonlinearities through vibro-impact are not always easy to control. Alternatively, nonlinearities through nonlinear electrical shunts may potentially offer an alternative to overcome this limitation. The tuning flexibility it offers would allow for tactic design of the shunts to cater for particular structural modes in specific frequency ranges. However, nothing has been reported in the context of ABH structures. It remains unclear whether the idea is feasible, and if so, what are the nonlinear features of the system and how they will impact the inherent physical process pertinent to ABH phenomena.

Motivated by the above, this paper targets a two-fold objective: (a) Using an improved semi-analytical electro-mechanical coupling model which allows the consideration of nonlinear shunt circuits annexed to a PZT-coated ABH beam, to carry out systematic analyses on the associated nonlinear behaviors of the coupled ABH system in order to explore the nonlinear electromechanical coupling characteristics of ABH beam; (b) to understand the underlying mechanisms of energy transfer caused by nonlinear electro-mechanical ABH beam to realize enhanced and broadband ABH effects. Besides, analyses are also conducted to understand the effects of major system parameters form the system coupling and energy transfer perspectives, so as to provide useful design and optimization guidelines to maximize the low-frequency benefit of the ABH.

The present work shows its novelty through the proposition of coupling an electrical nonlinearity with an ABH structure and the

findings of ABH-specific nonlinear phenomena associated with the underlying physical insights. The method proposed in this work constitutes the very first attempt to use nonlinear electromechanical coupling delivering controllable and tunable nonlinearities in an ABH structure. Through revealing dominant nonlinear phenomena specific to ABH structures, understanding their underlying mechanisms and finally achieving nonlinearity-induced energy transfer, the study shows the benefit of utilizing intentional nonlinearity to selectively break down the frequency barrier of linear ABH structures, which has long been considered as one of the bottlenecking problems in ABH research.

The rest of the paper is organized as follows. An improved nonlinear electro-mechanical ABH model based on a previous work is first presented. Analyses on the coupled ABH system are then conducted to understand the influence of PZT layout on the electromechanical coupling strength, alongside a brief discussion on the selection of linear circuit parameters. Next, numerical analyses are conducted to reveal the associated nonlinear behaviors, explore the broadband vibration reduction and understand the underlying physical mechanisms governing the energy transfer process. Moreover, the effects of different system parameters are also studied. Results show that the electromechanical coupling, albeit relatively weak, can still entail rich nonlinear phenomena in the ABH beam, including modal hardening and the generation of high-order harmonics. Analyses show two dominant energy transfer paths from low to high frequencies within the ABH beam as well as between the mechanical and electrical components, like a nonlinear energy sink. These two energy transfer paths collectively enhance the passive damping effects of the ABH beam at low frequencies along with an enhanced vibration attenuation. Influences of various system parameters on the expected nonlinear process pertinent to the enhanced ABH effects are discussed to guide the design of the nonlinear shunts.

2. Theoretical model

As shown in Fig. 1, the system under investigation consists of a beam undergoing flexural vibration when subject to a point force excitation $f_{ext}(t)$ at x_f. The beam, with a constant width b, is composed of an uniform portion with a constant thickness $2h_u$ and an ABH portion with variable power-law profiled thickness ($2h_b$) from x_u to l, i.e. $h_b(x) = \beta(L-x)^m$, followed by an extended platform with uniform thickness h_0 till L, with L denoting the total length of the beam. The extended platform enables prolonged ABH effects as demonstrated previously [10]. Besides, piezoelectric patches and viscoelastic damping layers, of constant thickness h_p and h_d, respectively, are symmetrically installed over the top and bottom surfaces of the beam. The whole system is therefore symmetrical with respect to the mid-line of the beam. Both ends of the beam are elastically supported by a rotational spring and a translational spring, the stiffness of which can be adjusted to mimic various boundary conditions. As a special case to be studied here, a cantilever beam can be simulated by assigning sufficient large values to k_{10} and k_{20} for the uniform end, and setting k_{1L} and k_{2L} to 0 at the free end of the ABH beam as detailed in [21,53].

In our previous paper [54], we have proposed a fully coupled electromechanical model based on Timoshenko ABH beam with PZT patches and a linear shunt circuit via Rayleigh-Ritz approach. Upon decomposing the out-of-plane displacement, $w(x, t)$, and the rotation angle, $\theta(x, t)$, of the beam into a set of assumed admissible shape functions (modified trigonometric functions with supplementary boundary smoothing terms as detailed in [54]), the corresponding temporal coordinates (packed into two unknown vectors $\mathbf{a}$ (t) and $\mathbf{b}(t)$), the kinetic energy, potential energy and the work done by the external force $\mathbf{f}(t)$ and electrical loading can all be mathematically expressed to form the Lagrangian of the system. Using Lagrange's equations, we can get the fully coupled electromechanical equations, cast into the following form:

$$(\boldsymbol{M}_{a1} + \boldsymbol{M}_{a2}) \cdot \ddot{\boldsymbol{a}}(t) + \boldsymbol{M}_{b1} \cdot \ddot{\boldsymbol{b}}(t) + (\boldsymbol{K}_{a1} + \boldsymbol{K}_{a2} + \boldsymbol{K}_{a3}) \cdot \boldsymbol{a}(t) + (\boldsymbol{K}_{b1} + \boldsymbol{K}_{b2}) \cdot \boldsymbol{b}(t) - \boldsymbol{\Theta}_1 \cdot v(t) = \boldsymbol{f}_{ext}(t) \tag{1}$$

$$\boldsymbol{M}_{b1} \cdot \ddot{\boldsymbol{a}}(t) + \boldsymbol{M}_{b2} \cdot \ddot{\boldsymbol{b}}(t) + (\boldsymbol{K}_{b1} + \boldsymbol{K}_{b2}) \cdot \boldsymbol{a}(t) + (\boldsymbol{K}_{b3} + \boldsymbol{K}_{b4} + \boldsymbol{K}_{b5}) \cdot \boldsymbol{b}(t) - \boldsymbol{\Theta}_2 \cdot v(t) = 0 \tag{2}$$

$$\boldsymbol{\Theta}_1^T \cdot \boldsymbol{a}(t) + \boldsymbol{\Theta}_2^T \cdot \boldsymbol{b}(t) + C_{eq} \cdot v(t) = q(t) \tag{3}$$
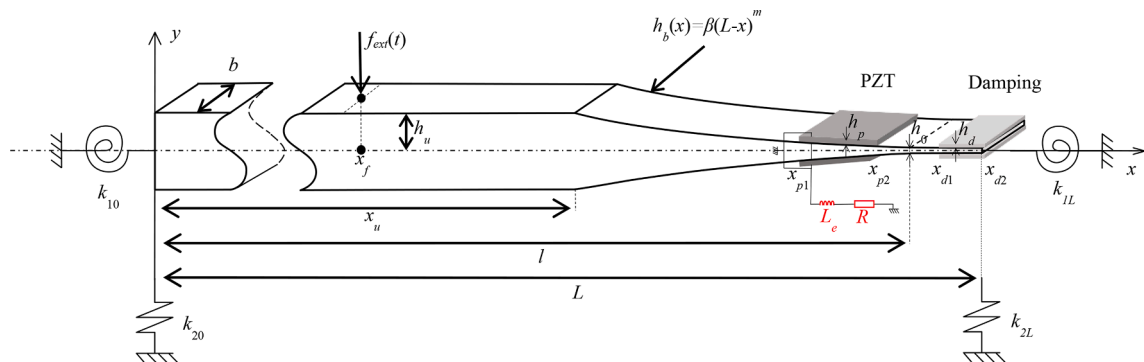

Fig. 1. A beam containing an ABH portion with symmetrical and power-law thickness profile with a uniform platform at its tip end (right end).

where $\mathbf{M}$ and $\mathbf{K}$ with subscripts stand for different components which form the global mass matrix and stiffness matrix. Similarly, $\boldsymbol{\Theta}$ is the electromechanical coupling matrix and C_{eq} the capacitance of the PZT equivalent circuit, the electromechanical coupling in the system is ensured via the electrical voltage $v(t)$. $\mathbf{T}$ denotes the transpose of a matrix. Details of these matrix components are provided in our previous paper [54].

As a further simplification for nonlinear solution, the above formulation based on Timoshenko theory is simplified to a Euler-Bernoulli model by neglecting the cross-sectional rotational inertia and shear deformation of the beam, whose effects on linear vibration behaviors have been thoroughly investigated [54]. That is, the coupled Eqs. (1)–(3) can be simplified to:

$$\mathbf{M} \cdot \ddot{\boldsymbol{a}}(t) + \mathbf{K} \cdot \boldsymbol{a}(t) - \boldsymbol{\Theta}_1 \cdot v(t) = \boldsymbol{f}_{ext}(t) \tag{4}$$

$$\boldsymbol{\Theta}_1^T \cdot \boldsymbol{a}(t) + C_{eq} \cdot v(t) = q(t) \tag{5}$$

where $\mathbf{M} = \mathbf{M}_{a1} + \mathbf{M}_{a2}$ and $\mathbf{K} = \mathbf{K}_{a1} + \mathbf{K}_{a2} + \mathbf{K}_{a3}$.

In the above formulation, any external circuit can be connected to the PZT patches as part of the whole electro-mechanical system, including both linear and nonlinear shunts. In the present case, a nonlinear oscillating circuit, including a cubic nonlinear capacitance, is used as shown in Fig. 2, governed by:

$$v(t) = L_e \cdot \ddot{q}(t) + R \cdot \dot{q}(t) + \frac{1}{C_{eq}} \cdot q(t) + \frac{1}{C_{nl}} \cdot q^3(t) \tag{6}$$

where L_e is the inductance, R is the resistance and C_{nl} is the nonlinear capacitance of the external circuit.

Substituting Eq. (6) into Eqs. (4) and (5), the fully coupled electromechanical ABH model with external nonlinear circuit can then be written in the following matrix form:

$$\begin{bmatrix} \mathbf{M} & \\ & L_e \end{bmatrix} \begin{bmatrix} \ddot{\boldsymbol{a}}(t) \\ \ddot{q}(t) \end{bmatrix} + \begin{bmatrix} image(\mathbf{K})/\omega & \\ & R \end{bmatrix} \begin{bmatrix} \dot{\boldsymbol{a}}(t) \\ \dot{q}(t) \end{bmatrix} + \begin{bmatrix} real(\mathbf{K}) + C_{eq}^{-1}\boldsymbol{\Theta}_1\boldsymbol{\Theta}_1^{\mathbf{T}} & -C_{eq}^{-1}\boldsymbol{\Theta}_1 \\ -C_{eq}^{-1}\boldsymbol{\Theta}_1 & C_{eq}^{-1} \end{bmatrix} \begin{bmatrix} \boldsymbol{a}(t) \\ q(t) \end{bmatrix} + \begin{bmatrix} \mathbf{0} & \\ & C_{nl}^{-1} \end{bmatrix} \begin{bmatrix} \mathbf{0} \\ q^3(t) \end{bmatrix} = \begin{bmatrix} \boldsymbol{f}_{ext}(t) \\ 0 \end{bmatrix} \tag{7}$$

In Eqs. (1) to (3) and (4) to (5), the structural damping of the beam and that of the damping layer are considered through introducing complex Young's modulus. This leads to complex $\mathbf{K}$ matrix shown in the above equations. Conversion is made to find the equivalent viscous damping for computational purposes.

In the subsequent numerical analyses, frequency domain solution is obtained using Harmonic Balance Continuation method [55], coupled with a continuation strategy, proven to be effective for solving multi-degree-of-freedom nonlinear problems. The periodic signals $\mathbf{x}(t) = [\boldsymbol{a}(t)\ q(t)]$ and $\mathbf{f}(\mathbf{x}, t) = [\boldsymbol{f}_l(t)\text{-}\boldsymbol{f}_{nl}(\mathbf{x})]$ (where $\boldsymbol{f}_l(t) = [\boldsymbol{f}_{ext}(t)\ 0]$) in Eq. (7) are approximated by Fourier series truncated to the N_H^{th} harmonic:

$$\boldsymbol{x}(t) = \boldsymbol{c}_0^x + \sum_{i=1}^{N_H} \left(\boldsymbol{s}_i^x \sin i\omega t + \boldsymbol{c}_i^x \cos i\omega t \right) \tag{8}$$

$$\boldsymbol{f}(t) = \boldsymbol{c}_0^f + \sum_{i=1}^{N_H} \left(\boldsymbol{s}_i^f \sin i\omega t + \boldsymbol{c}_i^f \cos i\omega t \right) \tag{9}$$

where $\mathbf{s}_i$ and $\mathbf{c}_i$ represent the vectors of the Fourier coefficients related to the sine and cosine terms of ith harmonic, respectively. These coefficients are gathered into the vectors to obtain the equations of the harmonic coefficient:

$$\boldsymbol{z} = \left[\left(\boldsymbol{c}_0^x\right)^T \ \left(\boldsymbol{s}_1^x\right)^T \ \left(\boldsymbol{c}_1^x\right)^T \dots \ \left(\boldsymbol{s}_{N_H}^x\right)^T \ \left(\boldsymbol{c}_{N_H}^x\right)^T \right]^T \tag{10}$$

$$\boldsymbol{d} = \left[\left(\boldsymbol{c}_0^f\right)^T \ \left(\boldsymbol{s}_1^f\right)^T \ \left(\boldsymbol{c}_1^f\right)^T \dots \ \left(\boldsymbol{s}_{N_H}^f\right)^T \ \left(\boldsymbol{c}_{N_H}^f\right)^T \right]^T \tag{11}$$
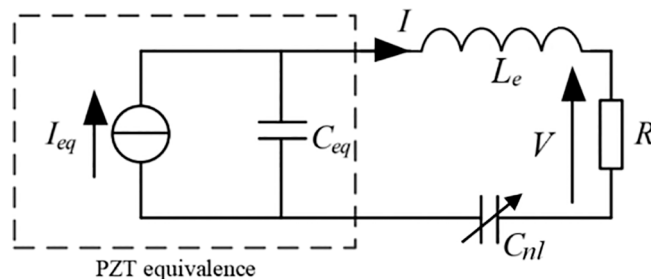

Fig. 2. Schematic diagram of external nonlinear circuit.

The displacements and forces are recast into a more compact form:

$$\boldsymbol{x}(t) = (\boldsymbol{Q}(t) \otimes \mathrm{II}_n) \cdot \boldsymbol{z} \tag{12}$$

$$\boldsymbol{f}(t) = (\boldsymbol{Q}(t) \otimes \mathrm{II}_n) \cdot \boldsymbol{d} \tag{13}$$

where $\otimes$ and II_n respectively present the Kronecker tensor product and the identity matrix of size n, and $\boldsymbol{Q}(t)$ is a vector containing the sine and cosine series as $[1 \; \sin\omega t \; \cos\omega t \; \dots \; \sin N_H \omega t \; \cos N_H \omega t]$. Accordingly, velocities and accelerations can also be defined using the Fourier series.

Substituting the new form of displacement, velocity, acceleration and force in the equations of motion (7), and considering the mixed-product property of the Kronecker tensor product, then Galerkin procedure is used to remove the time dependency and obtain an expression relating the different Fourier coefficients, the equations of motion expressed in the frequency domain are eventually obtained, written in a more compact form:

$$\boldsymbol{A}(\omega)\boldsymbol{z} - \boldsymbol{d}(\boldsymbol{z}) = \boldsymbol{0} \tag{14}$$

where $\boldsymbol{A}$ is the matrix describing the linear dynamics. Eq. (14) is nonlinear and has to be solved iteratively (e.g., with a Newton-Raphson procedure). At each iteration, an evaluation of $\boldsymbol{d}$ has to be provided, which can be computed by the alternating frequency/time-domain (AFT) technique:

$$\boldsymbol{z} \overset{\mathrm{FFT}^{-1}}{\to} \boldsymbol{x}(t) \to \boldsymbol{f}(\boldsymbol{x}, t) \overset{\mathrm{FFT}}{\to} \boldsymbol{d}(\boldsymbol{z}) \tag{15}$$

Besides, in the present work, the time domain solution is obtained by Newmark method, which is widely used in solving the nonlinear problems. Details on these numerical treatment are described in [56].

3. Numerical analyses

An electro-mechanical cantilever ABH beam is numerically investigated, with its material and geometrical parameters tabulated in Table 1. The ABH beam is subject to a harmonic point force excitation of 1 N in amplitude at the point $x_f = 0.1$ m on the uniform portion. Different observation positions on the beam (either on the uniform portion or the ABH portion) are used for structural response assessment. Calculations conducted using 16 decomposition terms plus auxiliary terms are shown to be enough to ensure converged results within the entire frequency range of interest investigated in this paper.

3.1. Coupling characteristics of the ABH beam with linear/nonlinear shunts

Numerical examples are given in the following sections to systematically illustrate the electromechanical coupling characteristics of the ABH beam with the shunted PZT and damping layers in different cases: without electrical shunts; with linear RL (resistance and inductance) oscillating circuit and with nonlinear circuit that includes a nonlinear capacitance on top of the linear circuit.

A commonly used metric to measure the effective range of the ABH effects is the cut-on frequency or the characteristic frequency of an ABH structure, denoted by f_c and defined as [54]:

$$f_c = \frac{2\pi h_u}{l_{\mathrm{ABH}}^2} \sqrt{\frac{E_b}{12\rho_b}} \tag{16}$$

Table 1
Material and geometrical parameters of the beam, PZT and electrical shunt.

Material parameters	Geometrical parameters
Beam	Beam
Density: $\rho_b = 7800$ kg/m^3	$\beta = 0.1$
Damping loss factor: $\eta_b = 0.005$	$m = 2$
Elasticity modulus: $E_b = 210$GPa	$b = 0.05$ m
Damping	$x_u = 0.25$ m
Density: $\rho_d = 950$ kg/m^3	$l = 0.45$ m
Damping loss factor: $\eta_d = 0.5$(case-specific)	$L = 0.5$ m
Elasticity modulus: $E_d = 5$GPa	$h_u = 6.25$ mm
PZT	$h_0 = 0.5$ mm
Density: $\rho_p = 7600$ kg/m^3	Damping
Damping loss factor: $\eta_p = 0$	$x_{d1} = 0.48$ m
Elasticity modulus: $E_p = 132$GPa	$x_{d2} = 0.5$ m
Piezoelectric stress constant: $e = -3$C/m^3	$h_d = 0.5$ mm
Dielectric constant: $\varepsilon^s = 2.8 \times 10^{-9}$F/m	PZT
Electrical shunt	$x_{p1} = 0.42$ m
Inductance: $L_e = 1.895$H (case-specific)	$x_{p2} = 0.48$ m
Resistance: $R = 50$ Ω	$h_p = 0.5$ mm

where l_{ABH} denotes the length of the ABH portion, which includes the portion with variable power-law profiled thickness and the extended platform with a uniform thickness. In the present case, the cut-on frequency of the ABH beam is 940 Hz. The ABH beam with piezoelectric patches and damping layers with open circuit contains seven modes below 2000 Hz. The natural frequencies as well as the corresponding modal shapes of these modes are shown in Fig. 3. Note the white backgrounds represent the uniform portion of the ABH beam, and the shadowed ones represent the ABH portion.

Fig. 3 shows that the ABH portion undergoes strong oscillations with the corresponding amplitudes greatly exceeding that of the uniform portion, especially for higher-order modes. This shows strong energy concentration around the ABH tip, which is a typical ABH feature and conducive to energy dissipation. Note the fifth mode at 993.8 Hz slightly exceeds the cut-on frequency (940 Hz), starting from which systematic ABH effects can be expected. Therefore, we choose the fourth mode before the cut-on frequency as the design and analysis target in the subsequent analyses. The fourth mode shape diagram shows that the beam deforms significantly within the area 420–480 mm where piezoelectric patches are placed. This arrangement is expected to generate strong electro-mechanical coupling between the PZT and the host beam.

(1) Effect of ABH beam with a linear circuit

The electro-mechanical coupling strength, measured in terms of how a specific structural mode is affected, can be quantified using an electromechanical coupling factor k, defined as [41]:

$$k^2 = \frac{\omega_{oc}^2 - \omega_{sc}^2}{\omega_{sc}^2} \tag{17}$$

where ω_{oc} and ω_{sc} are the angular natural frequencies of a given mode of the structure when the piezoelectric transducer is open-circuited and short-circuited, respectively.

Fig. 4 shows the variation of k for the first seven modes. Indeed, the current arrangement leads to a maximum k for the fourth mode, which justifies the installation location of the PZTs in the present area to effectively alter the fourth structural mode. Targeting the frequency of this structural mode, the corresponding linear resistance and inductance (RL) resonant shunt yields the optimal inductance value of around 1.895H, determined by:

$$L_e = \frac{1}{C_{eq}\omega_{oc}^2} \tag{18}$$

Using a sine sweeping excitation with an amplitude of 1 N, Fig. 5 shows the displacement response of the ABH beam with and without optimal linear RL circuit. The beam displacement is calculated at $x_m = 0.45$ m at the ABH portion, expressed in dB, namely $20\log_{10}(Displacement)$. While informing on the general dynamics of the system, the comparison curves in Fig. 5 also show typical dynamic absorber phenomenon. As expected, the local attenuation of the resonant peak requires a precise tuning of the electrical shunt parameters, namely the electrical resonance has to be tuned to the open-circuit natural frequency ω_{oc}. No noticeable changes can be observed on other untargeted and lower-order resonances. This alludes to the need of adding a nonlinear cubic capacitance on top of
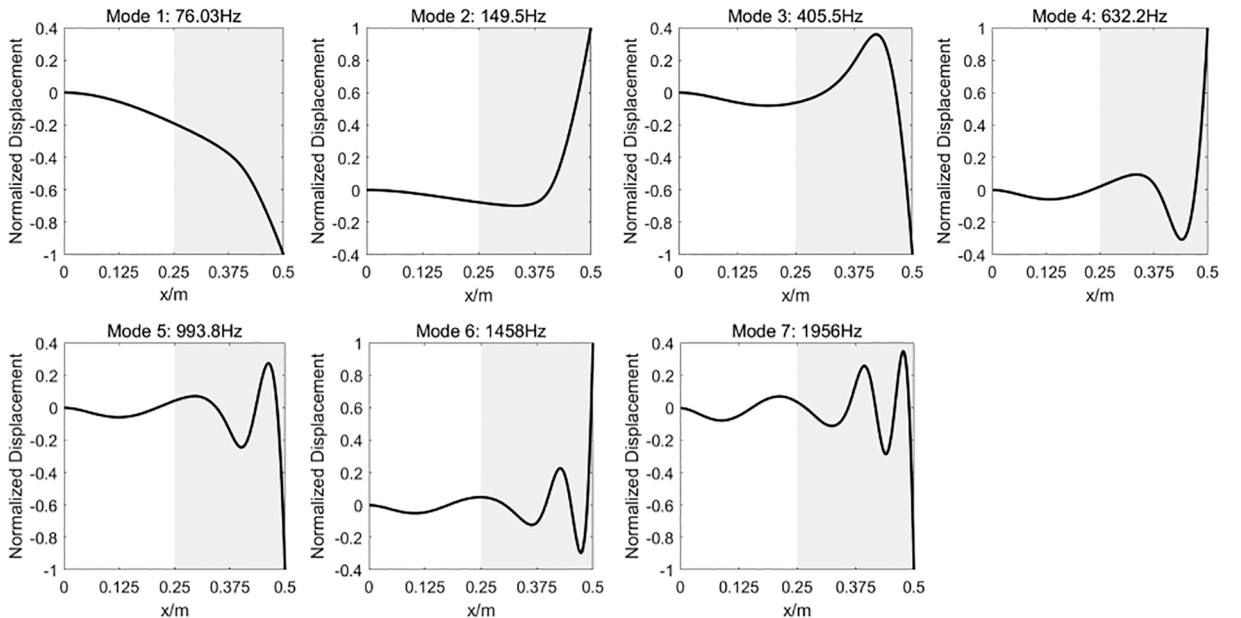

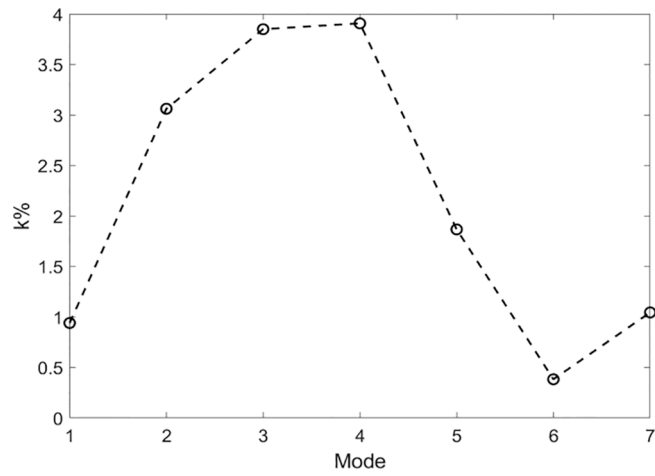**Fig. 3.** Modal shapes of the first seven modes below 2000 Hz.

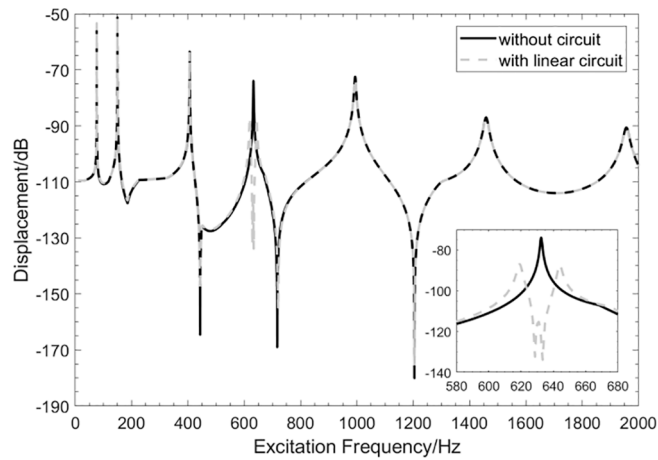**Fig. 4.** Electromechanical coupling factors of the first seven modes below 2000 Hz.

Fig. 5. Comparison of beam displacements placed PZT and damping layers without electrical shunt and with linear shunt.
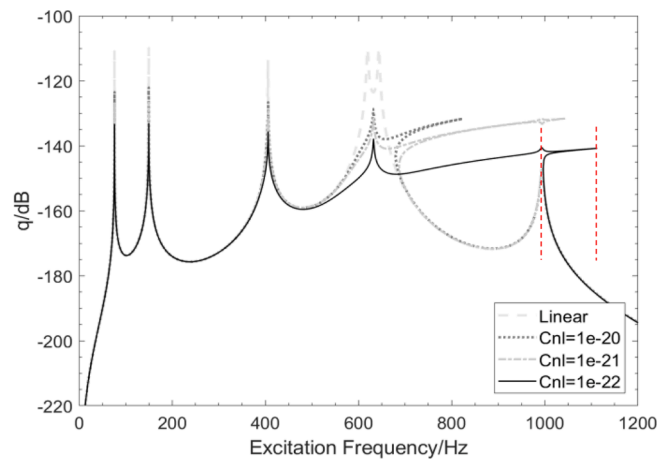

Fig. 6. Comparison of electrical charge amplitudes with linear shunt and different nonlinear shunt, in which the multiple solution region of curve $C_{nl} = 1e\text{-}22$ is marked by red dash lines.

the linear RL circuit to better promote ABH effects.

(2) Effect of ABH beam with nonlinear circuit

Having demonstrated the limitation of the linear RL oscillating circuit, we now add a nonlinear capacitance to the linear electrical shunt, with the capacitance value C_{nl} decreasing from $1 \times 10^{-20} C^3 V^{-1}$ to $1 \times 10^{-22} C^3 V^{-1}$. The evolution of the frequency–response diagram with different nonlinear capacitance would offer a good understanding on the nonlinear features of the coupled system, which facilitates the subsequent analyses in view of helping achieve enhanced ABH effects in a broader frequency range.

Fig. 6 shows the effect of the intentional electrical nonlinearity on the amplitude of the electrical charge q collected from the PZT patch. Several typical nonlinear phenomena are noteworthy. The first one is the hardening phenomenon due to the cubic nonlinear capacitance, reflected by an increase in the resonance frequency of the electrical resonance peak in the circuit, which bends to higher frequency to form a branch. As the nonlinearity increases (nonlinear capacitance decreases), the bending degree of the branch becomes larger until the merging with the neighboring higher-order resonance peak, which leads to a significant increase of the fifth resonance peak. Meanwhile, the use of nonlinear capacitance in the shunt also affects the dynamic absorber effect over the fourth peak (from mechanical system) due to the detuning effects from the nonlinear stiffness. As a result, the amplitude between the fourth and the fifth resonance peaks increases compared with the case with the linear shunt. Even when $C_{nl} = 1e\text{-}22$, the merging of the electrical reso-nance branch with the fifth resonance peak causes a high-energy frequency range between the fourth and fifth resonance peaks within which partial energy transfer might be expected (to be confirmed later). The second salient feature, also typical and common to nonlinear systems, is the existence of multiple solutions at some frequencies (take $C_{nl} = 1e\text{-}22$ as an example, the frequency range is marked between the red dash lines), the frequency range of the multiple solution region is consistent with the frequency range of the bending branch, which first increases with the increase of nonlinearity, until the bending branch merges with the next resonance peak, the range decreases. Note some solutions in these multiple solutions are unstable. Stability changes occur through bifurcations (in this case, fold bifurcations), which indicate a qualitative change in the dynamics of the system as system parameters are varied (in this case, the forcing frequency) [57]. Whether the system is on the high- or low-amplitude branch depends on its initial state. Finally, the amplitudes of the first four peaks undergo obvious reduction, suggesting a possibly reduced energy return from the mechanical system and an amplified low-frequency damping effect in the nonlinear shunt. Therefore, through the use of nonlinear capacitance, the electrical shunt exhibits hardening phenomenon near its resonant frequency, and the fact that the nonlinearity leads to more broadband energy transfer (expected effect of nonlinearity) is clearly visible in Fig. 6, which presents as energy reduction at lower-order mechanical resonant frequencies alongside a possible energy transfer from low to high frequencies. This will be further confirmed by subsequent analyses. By observing the evolution of the frequency–response diagram with different nonlinear capacitance values, one can notice that there is a critical capacitance value ($C_{nl} = 1e\text{-}21$) for which the electrical resonance branch starts to merge with the next resonance peak. A loop is formed at the fifth resonance peak, but isolated from the fifth resonance peak, which can be regarded to some extent as a detached resonance curve (DRC) which joins the main frequency response curve (FRC) [58,59]. Obvi-ously, DRC appears as an isolated loop of solutions in FRCs, whose detailed analysis is beyond the scope of the current study. For weaker nonlinearity than this critical value, the range of branch increases with the increase of nonlinearity. When the nonlinearity exceeds this critical value ($C_{nl} = 1e\text{-}22$), however, while the branch and the next resonance peak being merged, the range decreases. The trend of the multi-solution region is the same.

We now examine the corresponding changes in the mechanical system, by analyzing the displacement response of the beam and the generation of higher-order harmonics respectively.

Similar to the charge signals, due to the nonlinear capacitance, the linear resonant shunt-induced dynamic absorber effect (re-flected by the split of the fourth resonance peak) disappears. In addition, some nonlinear phenomena also appear on the beam, the most
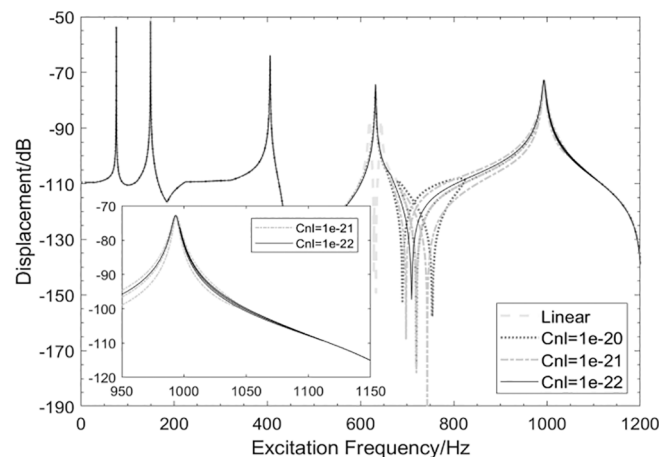

Fig. 7. Comparison of beam displacements with linear shunt and different nonlinear shunt.

obvious of which is that the bended and branch observed in Fig. 6 also appear in Fig. 7 as an isolated loop in the frequency response curves (FRCs). The branches manifest as a result of multi-valueless in the FRC, suggesting multiple solutions of the beam response under a harmonic excitation. A closer examination shows that the loop region coincides exactly with the unstable multi-solution region of the branch observed on q in Fig. 6, with similar variation trend. Meanwhile, we also observe in Fig. 7 that in the frequency range where loops appear, the nonlinear response of beam displacement is higher than the linear response. This phenomenon is also consistent with the charge curves in Fig. 6. It is relevant to note, however, that the phenomena observed in the beam are not as obvious as the ones on electrical charge due to the weak electromechanical coupling. In addition, we can see in the enlarged views (Fig. 8) that, compared with the linear case, the first three resonance peaks of the beam displacement response under nonlinear case also move, albeit slight, to higher frequencies. The amplitudes of the first three resonance peaks are also lower than the case without shunt. Though at a reduced level as compared with the electrical response, the use of nonlinear capacitance in the shunt seems to lead to an impaired low-frequency vibration response of the ABH beam, which results in slight resonance peak reduction in low frequencies.

Fig. 9 shows the effect of the electrical nonlinearity on the third harmonic in the mechanical system. In the figure, obvious nonlinear phenomena also appear. Firstly, compared with its linear counterpart, all of the first four resonance peaks produce obvious third harmonics, which should be accompanied by an energy increase in the high-frequency range. Secondly, similar to the electrical charge signals, near the fourth peak, other nonlinear features such as modal hardening and branch can also been observed. Increasing the strength of the nonlinearity (reduced nonlinear capacitance value) amplifies the hardening phenomenon and increases the amplitude of the third harmonic response. The outcome is the formation of a rather flattened and wide-band high-energy region between the fourth and the fifth resonances, in accordance with the merging of the branch formed by the bending of the fourth resonance peak towards higher frequency with the fifth resonance peak, already shown and discussed in Fig. 6. This means that not only obvious third-order harmonics of the resonant peaks are produced, but also obvious harmonics between the two, which is conducive to the enhanced energy transfer.

In the framework of this study, our attention is focused on the third harmonic because all other harmonics were found to be negligible, as exemplified in Fig. 10 (C_{nl} = 1e-21).

For more quantitative analysis, two indicators are defined to measure the strength of nonlinear phenomena. As shown in Fig. 11, taking the third-order harmonic curve with the nonlinear capacitance $C_{nl} = 1 \times 10^{-22} C^3 V^{-1}$ as an example, the first indicator quantifies the hardening degree in the nonlinear system, described by the frequency shift $\Delta f = f_q(\text{nonlinear}) - f_q(\text{linear})$, where $f_q(\text{linear})$ and $f_q(\text{nonlinear})$ are the electrical resonance frequencies with linear shunt and nonlinear shunt respectively. The second one is a measure
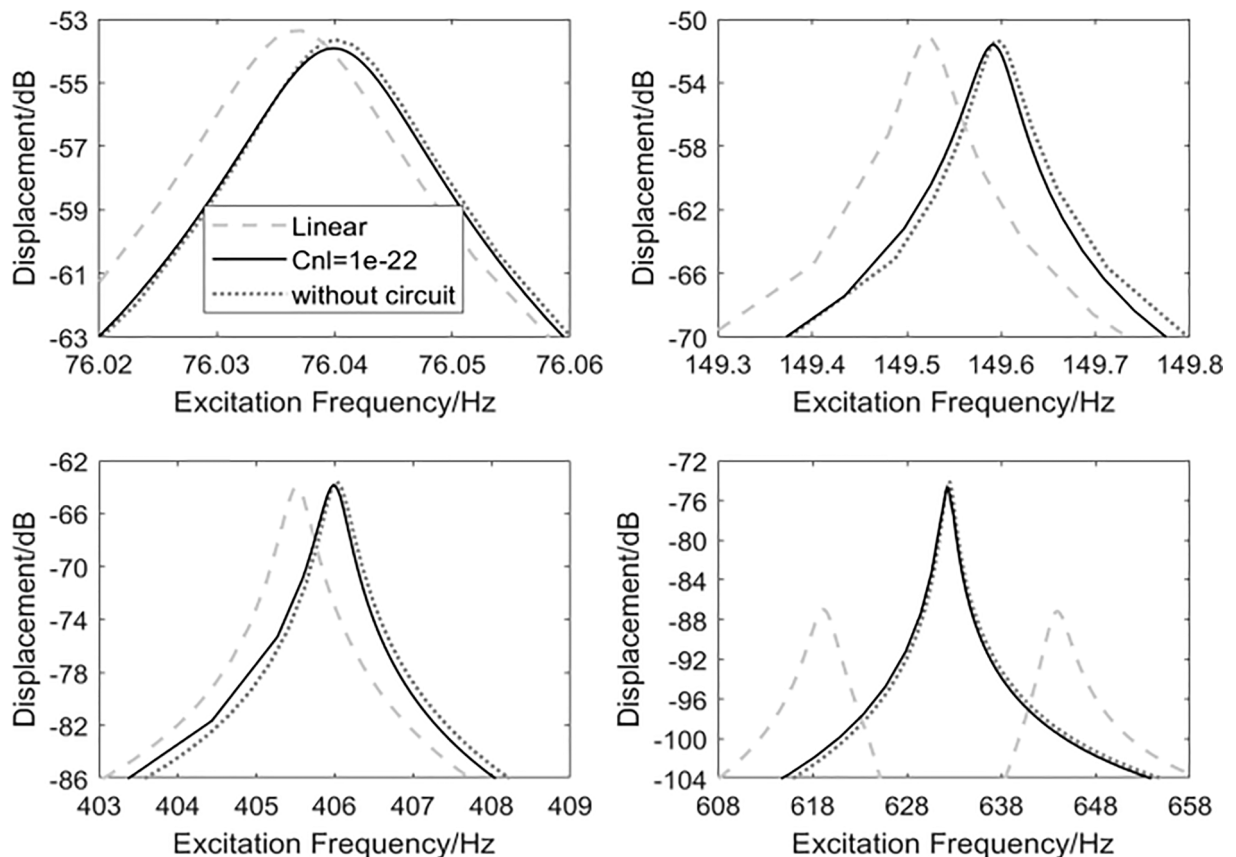

Fig. 8. Enlarged view of beam displacement without shunt, with linear shunt and with nonlinear shunt (C_{nl} = 1e-22) for the first four modes.
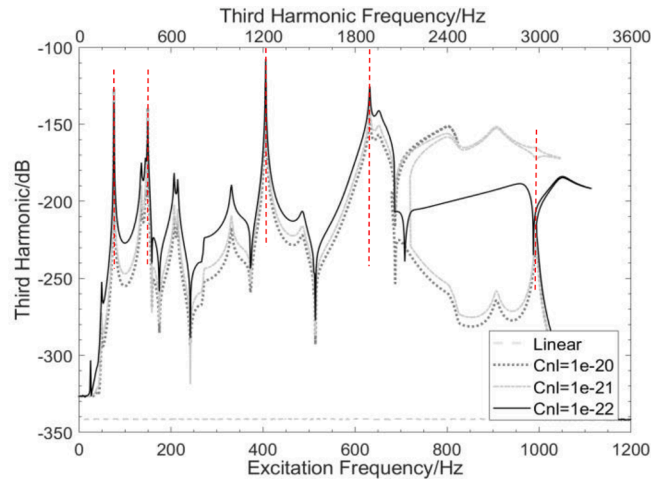
Fig. 9. Comparison of the third harmonics of beam with linear shunt and different nonlinear shunt, the lower abscissa represents the excitation frequencies, and the upper abscissa represents the third harmonic frequencies, the natural frequencies marked by red dash lines.
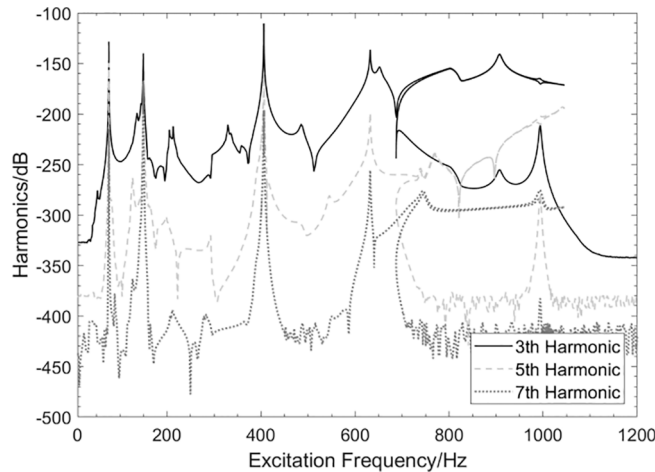

Fig. 10. Comparison of the different harmonics of beam with nonlinear shunt.

of the overall level of the third harmonics carried by the higher-order harmonics, which is defined as the integral area between the third harmonic curves of the nonlinear system and its linear counterpart, which can be understood as an indicator of energy transferred from the fundamental waves to the third harmonics, as marked by the shadowed region W in Fig. 11. The variation of Δf and W with different nonlinear capacitance value is respectively shown in Fig. 12(a) and (b).

It can be seen from Fig. 12 that both parameters, Δf and W, follow very similar variation trends, *i.e.*, increasing with nonlinearity strength (decreasing capacitance value). The greater the nonlinearity, the greater the degree of resonant peak bending, and the stronger the energy transfer from the fundamental waves to the third harmonics, as expected. The observation also points at the possibility of manipulating the energy transfer through a proper tuning of the nonlinear capacitance, which is easier to achieve than mechanical nonlinearity. It is also expected that the degree of the nonlinearity also increases with the excitation level so that similar changes in Δf and W could also be induced.

The above analyses suggest two possible mechanisms to realize low-to-high frequency energy transfer: through the formation of a branch/bridging of resonance modes as a result of hardening and through the generation of higher harmonics. The latter seems more significant than the former, which in principle might take place in nearly entire frequency band to different extent. This expected energy transfer process and its impact on ABH effects will be discussed in detail hereafter.

3.2. Energy transfer and enhanced ABH effects

Numerical examples are analyzed to confirm the aforementioned energy transfer phenomena caused by nonlinear shunt and the benefit they bring about in achieving enhanced ABH effects in different frequency bands. Beam response is calculated at $x_m = 0.45$ m,
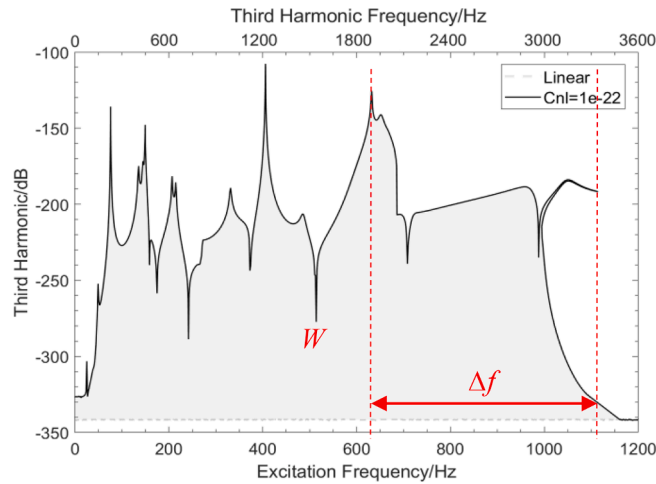
Fig. 11. A schematic diagram of two indicators defined to measure the strength of nonlinear phenomena. The bending degree of the circuit frequency Δf is marked by the red dash lines; W is the integral area between the third harmonic curves of the nonlinear system and its linear counterpart, marked by the shadowed region.
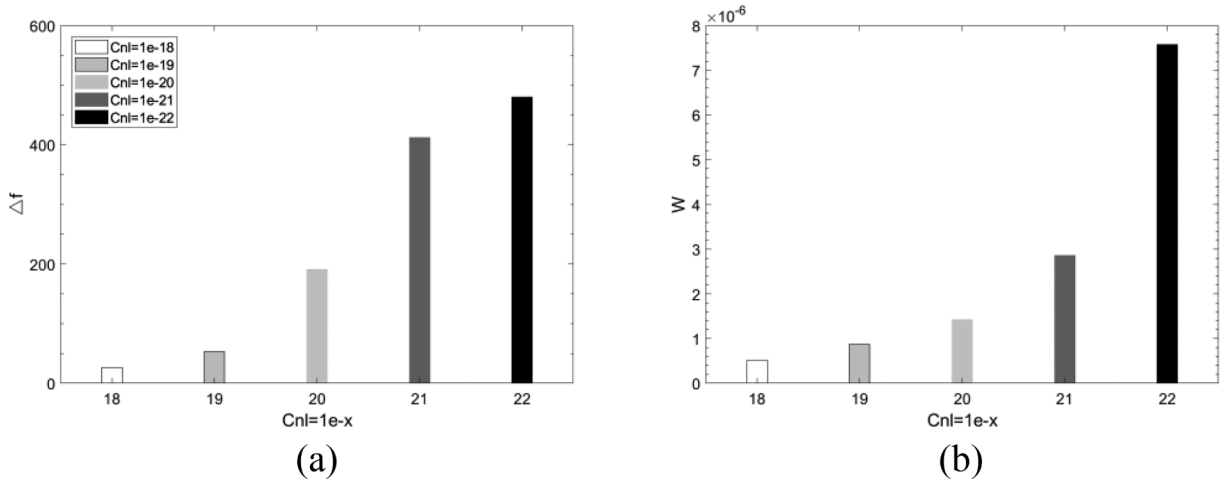

Fig. 12. Comparison of (a) Δf and (b) W with different nonlinear capacitances.

although other points (either on the uniform portion or the ABH portion closer to the tip) have also been verified to provide the same phenomena (not shown here).

(1) Energy transfer from low-to-high frequencies.

The considered excitation signal is based on a resonant decay. Harmonic forcing at a specific resonance frequency is applied first. After the response has reached steady state, the forcing amplitude is set to 0, and free vibration of the system ensues. Fast Fourier transform is then performed on the entire response signal to obtain the corresponding frequency-domain response, which can directly inform on the high-order harmonics (not only the third harmonics). The rationale behind is to produce a free vibration response which is initially dominated by one targeted mode and examine how the one-mode dominated energy could possibly be transferred to other frequencies in a free vibration regime. Note that while keeping the inherent material damping of the beam, the damping loss factor η_d of the damping layers is set to zero in order to show the phenomenon of energy transfer more clearly before it is dissipated later when the damping of the damping layer is added. Following the above procedure, the corresponding frequency spectra of the system are obtained.

In the present case, the ABH beam is successively excited at each of the first four natural frequencies (determined for the linear system) with a limited duration. Note they are all below the cut-on frequency of the ABH (Eq. (16)). The free response spectra corresponding to the four cases are shown in Fig. 13, in comparison with their respective linear counterparts. Note the junction between the white and the shadow regions indicates the ABH cut-on frequency, which is considered as a frequency barrier for producing

11

systematic ABH effects. It can be seen that, irrespective of the excitation frequency, high-order harmonics alongside other rather broadband energy intervals appear when the nonlinear capacitance is added in the circuit. Focusing more on Fig. 13(a) and (b), due to the higher vibration level dominated by the low frequency modes, a series of high-order harmonics appear more obviously. This causes an increase in the vibration level at higher frequencies alongside an amplitude reduction of the low-frequency peaks by different levels. In Fig. 13(c) and (d), due to the higher excitation frequency, there are fewer high-order harmonics within 2000 Hz. Nevertheless, it still leads to an increase of high-frequency energy and a decrease at low frequencies. It is relevant to note that, although Fig. 13(a-c) show peak reductions at and before the excitation frequency, their higher-order harmonics are still below the cut-on frequency of the ABH and thus cannot realize the sought cross ABH barrier energy transfer. Only the last case (Fig. 13(d)) allows meaningful and cross ABH barrier energy transfer with the generation of higher-order harmonics exceeding the cut-on frequency. Therefore, a meaningful cross ABH barrier energy transfer refers to the transfer of energy through higher-order harmonics from the region before the cut-on frequency of the ABH beam (white area) to the region after the cut-on frequency (shaded area).

The above analyses show that, the introduction of the electrical nonlinearity successfully generates broadband energy transfer from low to high frequencies, which is manifested by a decrease in low-frequency vibration and an increase in high-frequency energy. This completes and enriches the first step of the ABH process in terms of energy transport, namely a frequency domain energy transfer in addition to the spatial energy transport ensured by the ABH thickness variation. As the second ABH process, the increase of the high-frequency vibration energy in the system is expected to be dissipated by the damping of the coating layers, which is not considered in the above discussion. To verify this, the damping module is activated by considering its damping loss factor η_d. Fig. 14 shows the spectra corresponding to Fig. 13(d) with and without damping of the coating layer over the ABH tip. It can be seen that with damping η_d, the amplitudes of main resonance peaks are further reduced. More interestingly, in the high frequency region above the cut-on frequency and close to the third harmonic region, energy reduction is more obvious and significant. Note this is exactly the same frequency area into which energy was transferred owing to the electrical nonlinear shunt (Fig. 13(d)). The drastic energy reduction due to the damping layer is due to the ABH effects which are indeed enhanced and fully played out as a result of the intentionally added nonlinear electrical shunt. The entire process confirms that low-frequency energy (before the ABH barrier) is indeed transferred to higher frequencies (after the ABH barrier) before being more effectively dissipated through enhanced ABH effects. It is also worth noting that the low-frequency sub-harmonic peaks generated by the nonlinear electrical shunt also decrease significantly with the increase of η_d, such as the one-third sub-harmonic peak generated at around 200 Hz. The outcome of the entire process is the creation of better chance for the low frequency vibration to be reduced and ABH effects to be broadened, resulting in a simultaneous low- and
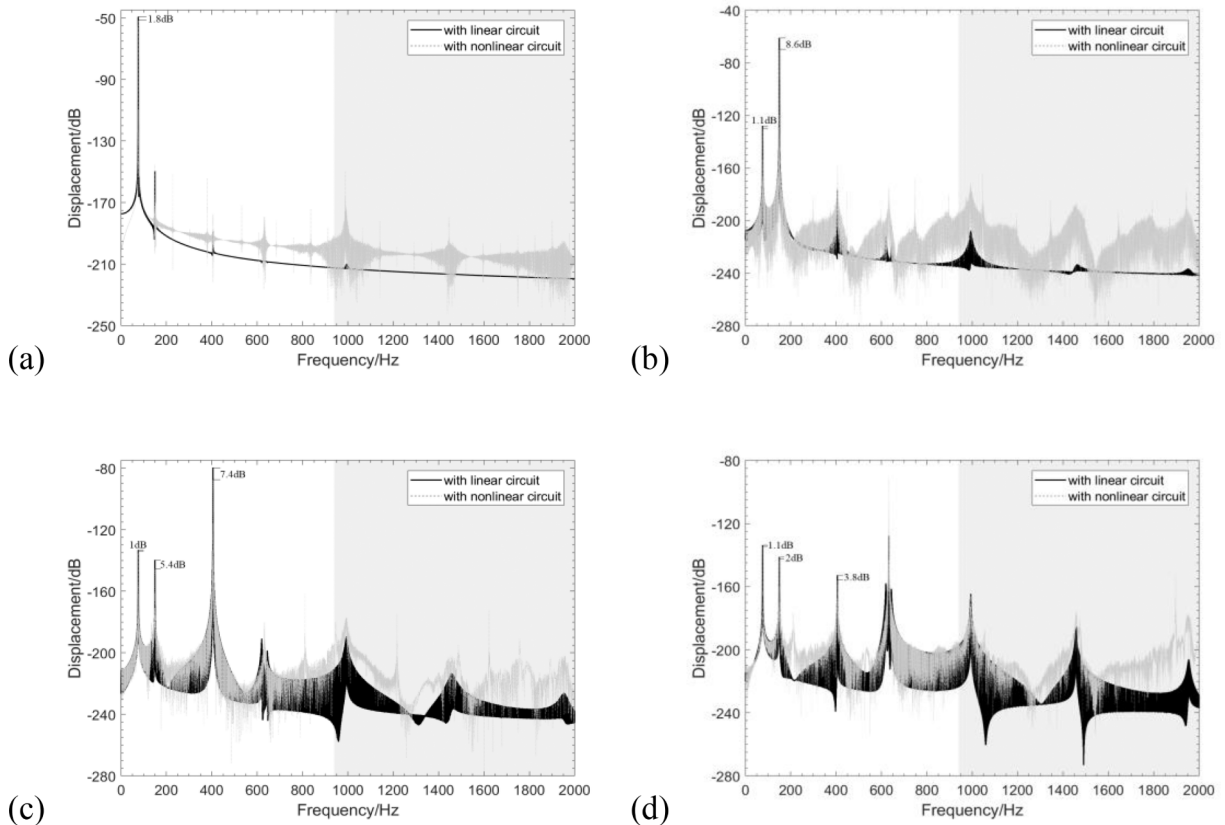

Fig. 13. Comparison of beam displacement spectra under single-frequency excitation forces with different frequencies: (a) 76.03 Hz; (b) 149.5 Hz; (c) 405.5 Hz; (d) 632.2 Hz.
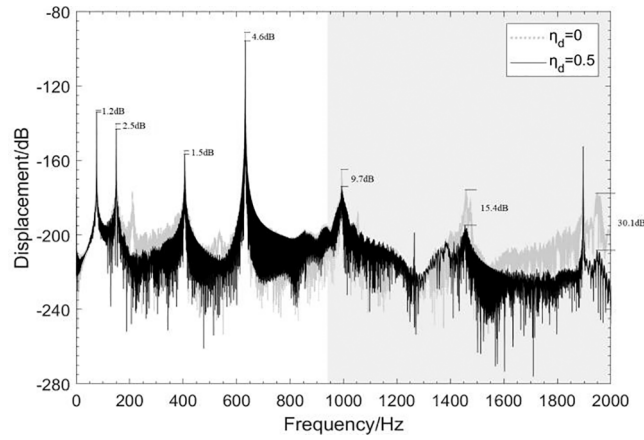
Fig. 14. Comparison of beam displacement spectra with different damping loss factor η_d under single-frequency excitation force at 632.2 Hz.

high-frequency vibration reduction.

In principle, the above observed energy dissipation is also partly from the introduced electrical shunt in addition to the ABH-induced dissipation. Calculations are conducted to separate these two components (electrical shunt and the damping layer) and quantify their respective contribution to the total energy dissipation. To this end, we first define power terms of different components in the system as:

$$P_d(t) = \dot{\boldsymbol{a}}(\boldsymbol{t}) \cdot \boldsymbol{C} \cdot \dot{\boldsymbol{a}}(\boldsymbol{t})^T \tag{19}$$

$$P_q(t) = v(t) \cdot \dot{q}(t) \tag{20}$$

$$P_f(t) = f(t) \cdot \dot{w}(x, t) \tag{21}$$

where $P_d(t)$, $P_q(t)$ and $P_f(t)$ represent the dissipated power by the damping layers, that of the electrical shunt and the input power of the force excitation, respectively. Their corresponding power spectra are obtained by Fast Fourier transform, denoted as P_d, P_q and P_f, respectively. The respective contributions of different power terms are assessed using.

$$P_d\% = \frac{P_d}{P_d + P_q} \times 100 \tag{22}$$

$$P_q\% = \frac{P_q}{P_d + P_q} \times 100 \tag{23}$$

Obviously, $P_d\%$ and $P_q\%$ represent respectively the relative portion of the energy dissipated mechanically and electrically.

Fig. 15 respectively shows the computed $P_d\%$ and $P_q\%$ in both full frequency range (Fig. 15(a)) and close-up view focusing on the higher frequency region (Fig. 15(b)) after a high pass filter above 1400 Hz is applied. Fig. 15(a) shows obvious energy dissipation by both the electrical shunt at its resonant frequency and its third-order harmonic. Due to the resonant nature of the circuit, however, system energy at other frequencies is mainly dissipated by mechanical damping (from both the beam and the damping layer). Focusing more on the high frequency range where effective energy transfer was observed before, Fig. 15(b) shows that, while electrical dissipation is present in the absence of the damping of the coating layer, especially towards the high-frequency end of the curves, the whole energy dissipation process is completely taken over and dominated by the damping layer after it is added to the system. This is particularly obvious in the broad region within which strong energy transfer is previously identified. In this frequency region, electrical damping contributes marginally, except near the third harmonics of the forcing frequency around 1900 Hz. These observations confirm that the vibration reduction at this high-frequency region is indeed due to the damping dissipation arising from the enhanced ABH effect.

(2) Energy transfer from mechanical-to-electrical system

In addition to the aforementioned energy transfer across frequency bands in the mechanical system, energy transfer also takes place from the ABH beam to the nonlinear electrical shunt, which is now investigated. Noting that the bridging of the fourth resonance peak with the fifth resonance peak, shown in Fig. 6, leads to a significant increase in the peak amplitude, we examine the associated nonlinear phenomena of the fifth structural mode. To this end, we examine the free vibration response of the beam. The onset of the system vibration is due to an initial force excitation at 993.8 Hz (fifth natural frequency of the beam) which is stopped after reaching steady state. The time-domain signals of the beam displacements, normalized to their respective maximum values, are shown in Fig. 16 (a). Corresponding $P_q(t)\%$ is used to quantify the percentage of energy transferred from the mechanical system to the electrical system
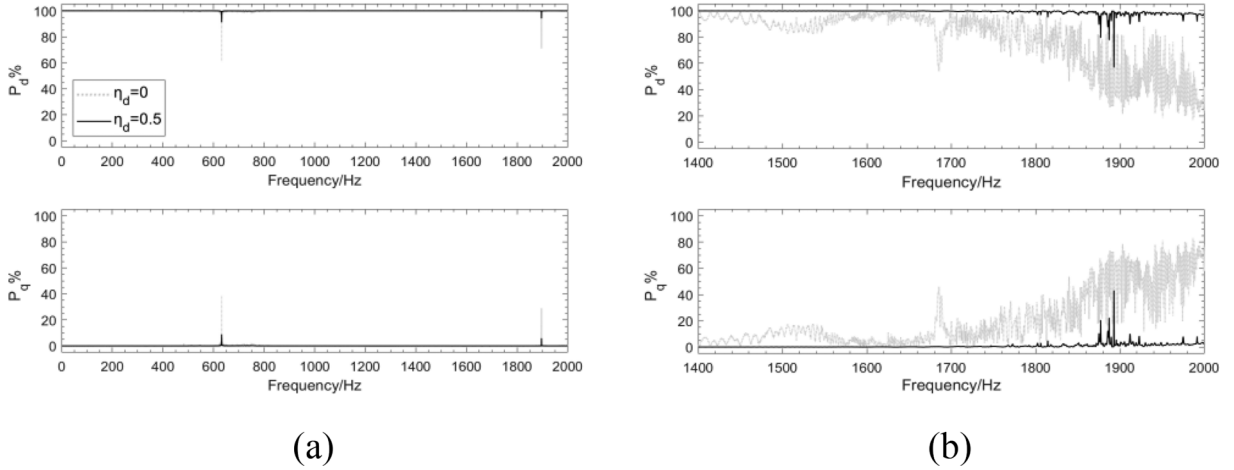
Fig. 15. Energy dissipation by damping layers and nonlinear electrical shunt for different η_d: (a) Broadband results; (b) Close-up view of higher frequency range after filtering.

in time domain, defined as.

$$P_q(t) \setminus \% \quad = \frac{P_q(t)}{P_f(t)} \times 100 \tag{24}$$

Fig. 16(a) shows an enlarged view of the free vibration response of the beam within a truncated time-window starting from $t = 2.14$ s (note the excitation for both cases stop at $t = 2$ s). Vibration response with electrical nonlinearity decays rapidly due to the enhanced damping effects. Roughly after $t = 2.2$ s, the nonlinear curve shows fluctuation with nevertheless significant signal attenuation. This instant roughly coincides with an obvious increase in the $P_q(t)\%$ as shown in Fig. 16(b), suggesting an increase in energy transfer to the electrical shunt. The fluctuation observed in Fig. 16(a) suggests a possible energy flow back to the beam, exemplified by a temporary increase, albeit slight, of the beam displacement at certain instants after $t = 2.22$ s. To better illustrate this phenomenon, a close-up of the time series in Fig. 17 reveals the existence of nonlinear beating. We see that the time between two successive maxima is decreasing over time, which indicates that the beating takes place between the excitation frequency, which coincides with the resonance frequency of the fifth mode, and another frequency which evolves with time. It turns out in Fig. 18 that this latter frequency is the resonance frequency of the fourth mode, which, due to the nonlinearity, is in the vicinity of the fifth mode before decreasing with motion amplitude. This is confirmed by the wavelet transform in Fig. 19. There is thus a vivid exchange of energy between modes 4 and 5. As a whole however, the energy transferred from the ABH beam to the electrical shunt dominates the process, which contributes to the rapid vibration attenuation of the beam alongside mechanical damping.

Numerical simulations also suggest that the level of the above mechanical–electrical energy transfer process does not monotonously increase with the nonlinearity strength (decreasing nonlinear capacitance values). This motivates us to examine the relationship between nonlinear capacitance and the amount of transferred energy from ABH beam to the electrical circuit, so as to optimize
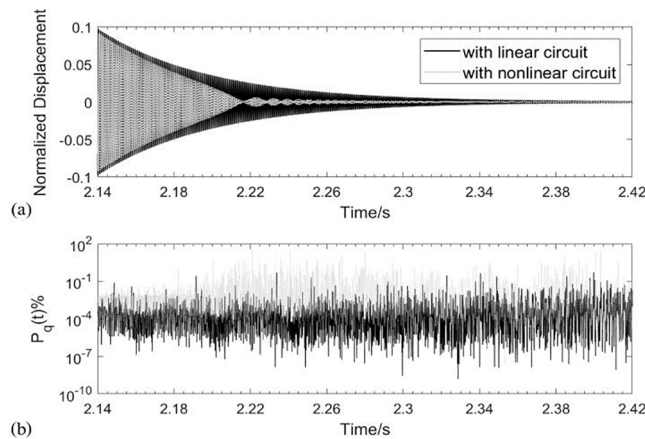

Fig. 16. Comparison of (a) normalized beam displacements and (b) the percentages of the circuit power to the total input power, when the excitation frequency is 993.8 Hz, $\eta_d = 0$.
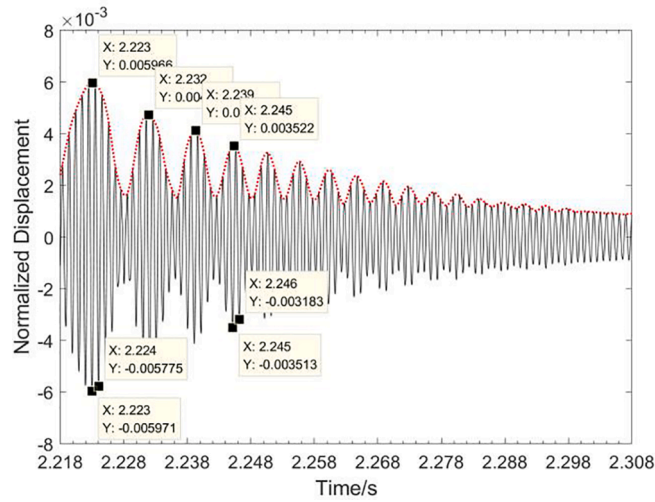
Fig. 17. Enlarged view of the normalized beam displacement in the beating region.
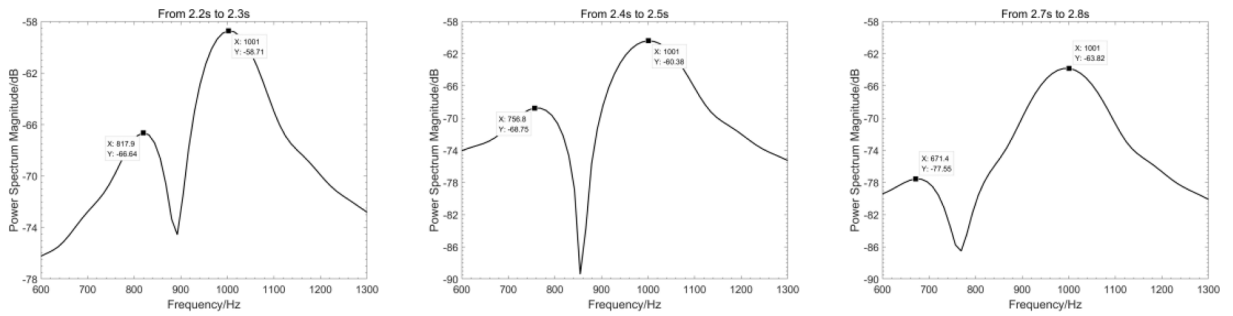

Fig. 18. Power spectral densities using different time series in the beating region.
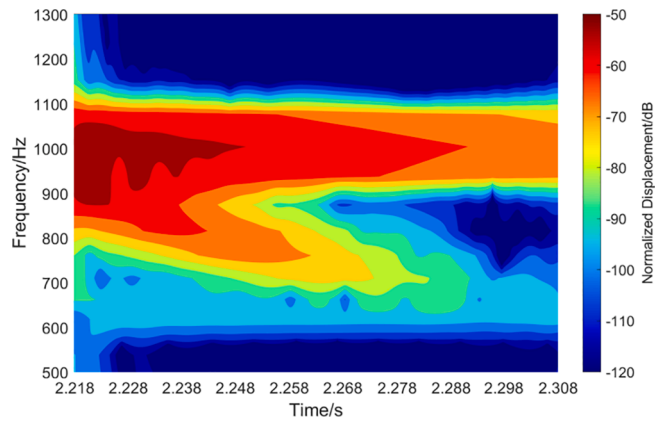

Fig. 19. Wavelet Transform Spectrum of the beam displacement in the beating region.

the circuit design to achieve the highest mechanical–electrical energy transfer efficiency. To quantify the process, we defining $W_q\%$ as.

$$W_q\% = \frac{W_q}{W_d + W_q} = \frac{\int_{t_1}^{t_2} P_q(t)dt}{\int_{t_1}^{t_2} P_d(t)dt + \int_{t_1}^{t_2} P_q(t)dt} \times 100 \tag{25}$$

Physically, $W_q\%$ represents the portion of the electrically dissipated energy over the total dissipated energy of the electrome-chanical system (the sum of energy dissipated by circuit W_q and energy dissipated by damping W_d) with a time duration delimited by

two time instants t_1 and t_2.

Variation of W_q% with respect to nonlinear capacitance C_{nl} is depicted in Fig. 20. It shows that electrical energy dissipation is the highest for a particular level of the nonlinearity. In addition, there exists a threshold nonlinearity level below which nearly no energy could be dissipated by the electrical shunt. This observation is also consistent with the nonlinear energy sink (NES) [33].

Note that all above analyses use an electrical nonlinear shunt whose linear resonant frequency f_q is designed to precisely target the fourth natural frequency of the beam. It is then relevant to comment on cases where f_q is not exactly tuned to match one particular mode. Numerical analyses show that as long as f_q is around the targeted mode, either below and above, basically the same phenomena as described above are still persistent, providing the flexibility and the tolerance for the design of the nonlinear electrical shunt.

4. Conclusions

This paper is concerned with intentionally imposing electrical nonlinearities via PZT patches over an ABH beam to tactically influence its dynamics through electromechanical coupling for achieving enhanced ABH effects. To this end, a previously established semi-analytical electromechanical coupling model is improved, which allows for the inclusion of a nonlinear shunt circuit annexed to an ABH beam. Salient nonlinear features in the electro-mechanical coupled system as well as major ABH-specific benefits are numerically demonstrated and physically explained.

It is shown that the introduction of electrical nonlinearity enables obvious and rich nonlinear phenomena in both the electrical and mechanical systems. For the former, the deployment of a cubic capacitance in the resonant shunt generates pronounced hardening phenomenon. The targeted resonance peak bends to higher frequency as a branch, which might even bridge/merge with the neighboring resonance peak provided the introduced nonlinearity is sufficiently strong. The process is accompanied by the creation of higher harmonics with energy transfer to higher frequencies in the circuit. As a result, the amplitudes of electrical resonances in the lower frequency range are reduced. Corresponding to the same frequency region, the branches observed in the electrical signal appear as an isolated loop in the frequency response curves (FRCs) of the ABH beam, which is shown to produce similar phenomena as a nonlinear energy sink (NES), in terms of generating energy transfer from the beam to the electrical circuit. Meanwhile obvious cross frequency energy transfer is also achieved. Although the phenomenon is not as obvious as in the electrical circuit due to the limited level of electromechanical coupling, it does lead to the low-frequency vibration reduction of the ABH beam, and most importantly, generates typical nonlinear phenomena which are vital for achieving low-to-high frequency energy transfer. Analyses show two dominant energy transfer paths within the ABH beam as well as between the mechanical and electrical components: one through the formation of a branch/bridging of resonance modes as a result of hardening and the other through the generation of higher harmonics. The latter is shown to be more compelling and predominant. These two energy transfer paths collectively alter the system dynamics, increase the ABH-specific energy focusing ability and enhance the passive damping effects of the ABH beam at lower frequencies.

Energy analyses also confirm the above physical process, particularly in relation to the energy dissipation by different components in the coupled electro-mechanical system. It is shown that the vibration reduction at high frequencies is indeed due to the damping dissipation, which is caused and amplified by the nonlinearity-enhanced ABH effects. In addition to the energy transfer across the ABH-imposed cut-on frequency barrier in the mechanical part, electro-mechanical energy transfer and dissipation also take place, similar to a NES. Among major features, a typical nonlinear beating phenomenon is observed, alongside a threshold nonlinearity level to trigger energy transfer from the ABH beam to the electrical circuit. This suggests that the nonlinearity level in the shunted resonant circuit needs to be properly tuned to reach the optimal configuration. While the system nonlinearity increases with the forcing level and decreases with the nonlinear capacitance, there is however no stringent requirement on the precise tuning of the resonant frequency of the electrical shunt, as long as it is around the natural frequency of structural mode which is targeted to achieve ABH-specific energy transfer.
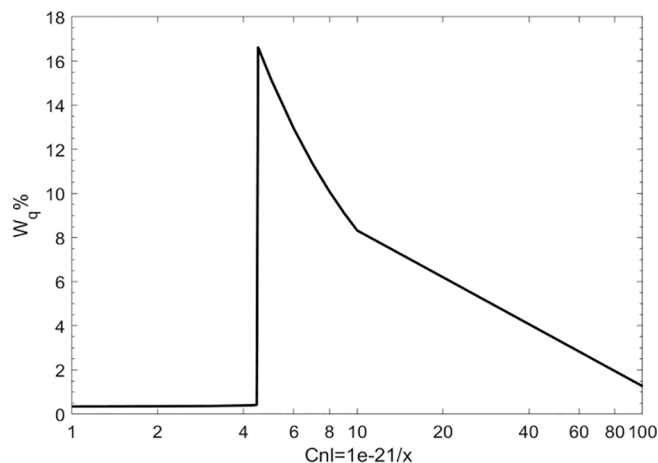

Fig. 20. Electrical energy dissipation with respect to C_{nl}.

Declaration of Competing Interest

The authors declare that they have no known competing financial interests or personal relationships that could have appeared to influence the work reported in this paper.

Acknowledgements

References

[1] M. Mironov, Propagation of a flexural wave in a plate whose thickness decreases smoothly to zero in a finite interval, Sov. Phys. Acoust. 34 (1988) 318–319.
[2] A. Pelat, F. Gautier, S.C. Conlon, F. Semperlotti, The acoustic black hole: A review of theory and applications, J. Sound Vib. 476 (2020) 115316.
[3] H. Ji, W. Huang, J. Qiu, L. Cheng, Mechanics problems in application of acoustic black hole structures, Adv. Mech. 47 (2017) 333.
[4] V.V. Krylov, Localized acoustic modes of a quadratic solid wedge, Mosc. Univ. Phys. Bull. 45 (1990) 65–69.
[5] V.V. Krylov, On the velocities of localized vibration modes in immersed solid wedges, J. Acoust. Soc. Am. 103 (1998) 767–770.
[6] V.V. Krylov, New type of vibration dampers utilising the effect of acoustic'black holes', Acta Acust united Ac. 90 (2004) 830–837.
[7] D. O'Boy, V.V. Krylov, Damping of flexural vibrations in circular plates with tapered central holes, J. Sound Vib. 330 (2011) 2220–2236.
[8] J. Deng, L. Zheng, P. Zeng, Y. Zuo, O. Guasch, Passive constrained viscoelastic layers to improve the efficiency of truncated acoustic black holes in beams, Mech. Syst. Sig. Process. 118 (2019) 461–476.
[9] H. Ji, J. Luo, J. Qiu, L. Cheng, Investigations on flexural wave propagation and attenuation in a modified one-dimensional acoustic black hole using a laser excitation technique, Mech. Syst. Sig. Process. 104 (2018) 19–35.
[10] L. Tang, L. Cheng, Enhanced acoustic black hole effect in beams with a modified thickness profile and extended platform, J. Sound Vib. 391 (2017) 116–126.
[11] T. Zhou, L. Cheng, A resonant beam damper tailored with acoustic black hole features for broadband vibration reduction, J. Sound Vib. 430 (2018) 174–184.
[12] P.A. Feurtado, S.C. Conlon, Transmission loss of plates with embedded acoustic black holes, J. Acoust. Soc. Am. 142 (2017) 1390–1398.
[13] L. Ma, L. Cheng, Sound radiation and transonic boundaries of a plate with an acoustic black hole, J. Acoust. Soc. Am. 145 (2019) 164–172.
[14] L. Zhao, S.C. Conlon, F. Semperlotti, Broadband energy harvesting using acoustic black hole structural tailoring, Smart Mater. Struct. 23 (2014) 065021.
[15] H. Ji, Y. Liang, J. Qiu, L. Cheng, Y. Wu, Enhancement of vibration based energy harvesting using compound acoustic black holes, Mech. Syst. Sig. Process. 132 (2019) 441–456.
[16] V. Krylov, Geometrical-acoustics approach to the description of localized vibrational modes of an elastic solid wedge, Sov. Phys. Tech. Phys. 25 (1990) 137–140.
[17] V. Krylov, F. Tilman, Acoustic 'black holes' for flexural waves as effective vibration dampers, J. Sound Vib. 274 (2004) 605–619.
[18] O. Guasch, M. Arnela, P. Sánchez-Martín, Transfer matrices to characterize linear and quadratic acoustic black holes in duct terminations, J. Sound Vib. 395 (2017) 65–79.
[19] X. Li, Q. Ding, Sound radiation of a beam with a wedge-shaped edge embedding acoustic black hole feature, J. Sound Vib. 439 (2019) 287–299.
[20] D. O'Boy, V.V. Krylov, Vibration of a rectangular plate with a central power-law profiled groove by the Rayleigh-Ritz method, Appl. Acoust. 104 (2016) 24–32.
[21] L. Tang, L. Cheng, H. Ji, J. Qiu, Characterization of acoustic black hole effect using a one-dimensional fully-coupled and wavelet-decomposed semi-analytical model, J. Sound Vib. 374 (2016) 172–184.
[22] S.C. Conlon, J.B. Fahnline, F. Semperlotti, Numerical analysis of the vibroacoustic properties of plates with embedded grids of acoustic black holes, J. Acoust. Soc. Am. 137 (2015) 447–457.
[23] L. Zhao, F. Semperlotti, Embedded acoustic black holes for semi-passive broadband vibration attenuation in thin-walled structures, J. Sound Vib. 388 (2017) 42–52.
[24] P.A. Feurtado, S.C. Conlon, An experimental investigation of acoustic black hole dynamics at low, mid, and high frequencies, J. Vib. Acoust. 138 (2016).
[25] E. Bowyer, V.V. Krylov, Experimental study of sound radiation by plates containing circular indentations of power-law profile, Appl. Acoust. 88 (2015) 30–37.
[26] E. Bowyer, D. O'Boy, V.V. Krylov, F. Gautier, Experimental investigation of damping flexural vibrations in plates containing tapered indentations of power-law profile, Appl. Acoust. 74 (2013) 553–560.
[27] V.V. Krylov, Acoustic black holes: recent developments in the theory and applications, IEEE Trans. Ultrason. Ferroelectr. Freq. Control 61 (8) (2014) 1296–1306.
[28] B.M.P. Chong, L.B. Tan, K.M. Lim, H.P. Lee, A review on acoustic black-holes (ABH) and the experimental and numerical study of ABH-featured 3D printed beams, Int. J. Appl. Mech. 9 (2017) 1750078.
[29] L. Tang, L. Cheng, Ultrawide band gaps in beams with double-leaf acoustic black hole indentations, J. Acoust. Soc. Am. 142 (2017) 2802–2807.
[30] J.Y. Lee, W. Jeon, Vibration damping using a spiral acoustic black hole, J. Acoust. Soc. Am. 141 (2017) 1437–1445.
[31] S. Mohanty, S.K. Dwivedy, Linear and nonlinear analysis of traditional and non-traditional piezoelectric vibration absorber with time delay feedback for simultaneous resonance conditions, Mech. Syst. Sig. Process. 161 (2021) 107980.
[32] F. Georgiadis, A.F. Vakakis, D.M. McFarland, L. Bergman, Shock isolation through passive energy pumping caused by nonsmooth nonlinearities, Int. J. Bifurc. Chaos 15 (2005) 1989–2001.
[33] A.F. Vakakis, O.V. Gendelman, L.A. Bergman, D.M. McFarland, G. Kerschen, Y.S. Lee, Nonlinear targeted energy transfer in mechanical and structural systems, Springer Science & Business Media, 2009.
[34] K. Asadi, J. Yu, H. Cho, Nonlinear couplings and energy transfers in micro-and nano-mechanical resonators: intermodal coupling, internal resonance and synchronization, Philos. Trans. Royal Soc. A 376 (2018) 20170141.
[35] K. Vorotnikov, Y. Starosvetsky, Nonlinear energy channeling in the two-dimensional, locally resonant, unit-cell model. I. High energy pulsations and routes to energy localization, Chaos 25 (2015) 073106.
[36] A.H. Nayfeh, D.T. Mook, P. Holmes, Nonlinear oscillations, Wiley, New York, 1979.
[37] A.H. Nayfeh, R.A. Ibrahim, Nonlinear interactions: analytical, computational, and experimental methods, Appl. Mech. Rev. 54 (4) (2001) B60–B61.
[38] F. Nucera, A.F. Vakakis, D. McFarland, L. Bergman, G. Kerschen, Targeted energy transfers in vibro-impact oscillators for seismic mitigation, Nonlinear Dyn. 50 (2007) 651–677.
[39] F. Nucera, F. Lo Iacono, D.M. McFarland, L.A. Bergman, A.F. Vakakis, Application of broadband nonlinear targeted energy transfers for seismic mitigation of a shear frame: Experimental results, J. Sound Vib. 313 (1-2) (2008) 57–76.
[40] E. Gourc, G. Michon, S. Seguy, A. Berlioz, Experimental investigation and design optimization of targeted energy transfer under periodic forcing, J. Vib. Acoust. 136 (2014).
[41] G. Raze, A. Jadoul, S. Guichaux, V. Broun, G. Kerschen, A digital nonlinear piezoelectric tuned vibration absorber, Smart Mater. Struct. 29 (2019) 015007.
[42] G.S. Agnes, D.J. Inman, Nonlinear piezoelectric vibration absorbers, Smart Mater. Struct. 5 (5) (1996) 704–714.
[43] C. Richard, D. Guyomar, D. Audigier, H. Bassaler, Enhanced semi-passive damping using continuous switching of a piezoelectric device on an inductor, Smart structures and materials 2000: damping and isolation, International Society for Optics and Photonics, 2000, pp. 288-299.
[44] B. Lossouarn, J.-F. Deü, G. Kerschen, A fully passive nonlinear piezoelectric vibration absorber, Philos. Trans. Royal Soc. A 376 (2018) 20170142.
[45] S.L. Feudo, C. Touzé, J. Boisson, G. Cumunel, Nonlinear magnetic vibration absorber for passive control of a multi–storey structure, J. Sound Vib. 438 (2019) 33–53.

[46] T.M. Silva, M.A. Clementino, C. De Marqui Jr, A. Erturk, An experimentally validated piezoelectric nonlinear energy sink for wideband vibration attenuation, J. Sound Vib. 437 (2018) 68–78.

[47] X. Zhang, H. Yu, Z. He, G. Huang, Y. Chen, G. Wang, A metamaterial beam with inverse nonlinearity for broadband micro-vibration attenuation, Mech. Syst. Sig. Process. 159 (2021) 107826.

[48] V. Denis, A. Pelat, C. Touzé, F. Gautier, Improvement of the acoustic black hole effect by using energy transfer due to geometric nonlinearity, Int. J. Non-Linear Mech. 94 (2017) 134–145.

[49] V.E. Gusev, C. Ni, A. Lomonosov, Z. Shen, Propagation of flexural waves in inhomogeneous plates exhibiting hysteretic nonlinearity: Nonlinear acoustic black holes, Ultrasonics 61 (2015) 126–135.

[50] H. Li, C. Touzé, A. Pelat, F. Gautier, X. Kong, A vibro-impact acoustic black hole for passive damping of flexural beam vibrations, J. Sound Vib. 450 (2019) 28–46.

[51] H. Li, C. Touzé, F. Gautier, A. Pelat, Linear and nonlinear dynamics of a plate with acoustic black hole, geometric and contact nonlinearity for vibration mitigation, J. Sound Vib. 508 (2021) 116206.

[52] H. Li, M. Sécail-Géraud, A. Pelat, F. Gautier, C. Touzé, Experimental evidence of energy transfer and vibration mitigation in a vibro-impact acoustic black hole, Appl. Acoust. 182 (2021) 108168.

[53] Y. Wang, J. Du, L. Cheng, Power flow and structural intensity analyses of acoustic black hole beams, Mech. Syst. Sig. Process. 131 (2019) 538–553.

[54] L. Zhang, G. Kerschen, L. Cheng, Electromechanical Coupling and Energy Conversion in a PZT-Coated Acoustic Black Hole Beam, Int. J. Appl. Mech. 12 (2020) 2050095.

[55] T. Detroux, L. Renson, L. Masset, G. Kerschen, The harmonic balance method for bifurcation analysis of large-scale nonlinear mechanical systems, Comput. Methods Appl. Mech. Eng. 296 (2015) 18–38.

[56] S.-Y. Chang, Studies of Newmark method for solving nonlinear systems: (I) basic analysis, J. Chin. Inst. Eng. 27 (5) (2004) 651–662.

[57] R. Seydel, Practical bifurcation and stability analysis, Springer Science & Business Media, 2009.

[58] G. Gatti, M.J. Brennan, I. Kovacic, On the interaction of the responses at the resonance frequencies of a nonlinear two degrees-of-freedom system, Phys. D: Nonlinear Phenomena 239 (10) (2010) 591–599.

[59] Y. Starosvetsky, O.V. Gendelman, Response regimes of linear oscillator coupled to nonlinear energy sink with harmonic forcing and frequency detuning, J. Sound Vib. 315 (2008) 746–765.